Fuel-lean ammonia/biogas combustion characteristics under the reacting swirl flow conditions

Guo Ren Mong[a], Meng-Choung Chiong[b,*], Cheng Tung Chong[c], Jo-Han Ng[d], Syed Mashruk[e], Manh-Vu Tran[f], Nor Afzanizam Samiran[g], Keng Yinn Wong[h], Agustin Valera-Medina[e]

[a] School of Energy and Chemical Engineering, Xiamen University Malaysia, 43900 Sepang, Selangor, Malaysia
[b] Department of Mechanical Engineering, Faculty of Engineering, Technology & Built Environment, UCSI University, 56000 Kuala Lumpur, Malaysia.
[c] China-UK Low Carbon College, Shanghai Jiao Tong University, Lingang, Shanghai 201306, China.
[d] Faculty of Engineering and Physical Sciences, University of Southampton Malaysia (UoSM), 79200 Iskandar Puteri, Johor, Malaysia.
[e] College of Physical Sciences and Engineering, Cardiff University, Wales, United Kingdom.
[f] School of Engineering, Monash University Malaysia, Jalan Lagoon Selatan, 47500 Bandar Sunway, Selangor, Malaysia.
[g] Department of Mechanical Engineering Technology, Faculty of Engineering Technology, Universiti Tun Hussein Onn Malaysia, 84600 Pagoh, Johor, Malaysia.
[h] School of Mechanical Engineering, Faculty of Engineering, Universiti Teknologi Malaysia, Skudai 81310, Johor, Malaysia.

Abstract

Ammonia has been identified as a viable energy vector for power generation. Using dual-fuel operation that mixes the ammonia with higher reactivity gaseous fuel can be vital in enhancing ammonia combustion. This study examined the fundamental swirl combustion characteristics of fuel-lean premixed ammonia/biogas via a numerical approach. The flame was established at an input thermal power of 7 kW and a global equivalence ratio of 0.8. The numerical model was verified and validated with biogas emissions data acquired through experimental work. At the 20 mm burner downstream, increased carbon dioxide mass fraction in the biogas lowered the peak flame temperature up to ~400 K. Moreover, the deformation of flame temperature radial profiles was also found aggravated as carbon dioxide concentration in the biogas elevated from 0% to 40%. The reduction in premixed reactant mixture reactivity not only initiated flame temperature profile deformation but also reduced the peak Damkhöler number significantly. The peak Damkhöler number was lowered by a factor of ~1.5 when carbon dioxide dilution in the biogas elevated by 40%. The premixed combustion was directed into the thin reaction flamelets zone with elevated carbon dioxide mass fraction, owing to the intensified flow fluctuation. This, in turn, gave rise to the average flow velocities, turbulent kinetic energy, and normalised turbulent flame speed, notwithstanding that heat release rate and laminar flame propagation declined. In all, the presence of carbon dioxide has been shown to lower the ammonia/methane mixture reactivity whilst escalating the reacting flow fluctuation.

Keywords: Ammonia; biogas; swirl combustion; premixed combustion; dual fuel

*Corresponding author
Address: Department of Mechanical Engineering, Faculty of Engineering, Technology & Built Environment, UCSI University, 56000 Kuala Lumpur, Malaysia.
Email: chiongmc@ucsiuniversity.edu.my ; mcchiong@outlook.com (MC Chiong)

1.0 Introduction

Carbon-free molecules like hydrogen (H_2) and ammonia (NH_3) are identified as potential substitutes for traditional carbon-based energy sources to mitigate global carbon emissions [1]. H_2 is an appealing carbon-free molecule, but its storage is challenging and pricey. On the contrary, the energy density of NH_3 is inherently greater than that of H_2. Furthermore, storage and transportation cost for NH_3 is also substantially more economic than for H_2 [2]. During the energy crises of the 1960s and 1970s, ammonia was temporarily used as transportation fuel [3]. Since the previous decade, initiatives to accelerate global carbon reduction have once more prioritised NH_3 as a viable alternative fuel, extending its use in direct-combustion-based power production and transportation fuel [2]. However, challenges are encountered when fuelling power generation machines with ammonia.

Due to ammonia's lower flammability than fossil fuels, it was shown that considerably greater ignition energy was needed to ignite the chemical [4]. At operation near the stoichiometric conditions, the minimum ignition energy for the NH_3/air mixture was ~21.5 times greater than the premixed propane (C_3H_8)/air mixture [5]. However, it was also observed that disassociated ammonia into hydrogen at ~28% could enhance the ammonia/air combustion, thus the minimum ignition energy was lowered by approximately two orders of magnitude [5]. Ammonia's flammability limit is likewise substantially narrower than that of H_2 and methane (CH_4). Methane and hydrogen can operate in a broader equivalence ratio (φ) range of 0.5-1.7 and 0.1-7.1, respectively. NH_3, however, can only operate within an equivalence ratio of 0.63-1.40 [6]. Owing to ammonia exhibiting lower flame stability than propane, a broader quenching distance is required for ammonia flame propagation at a global equivalence ratio of 0.8, a value that is around 50 mm broader than that for C_3H_8/air flame propagation [6]. To expedite ammonia as a greener fuel for upcoming power generation, elevating ammonia combustion quality along with minimal toxic emissions are crucial.

To enhance the combustion of neat ammonia, CH_4 was suggested as one of the potential solutions. Valera-Medina et al. [7] used a common swirl burner to study premixed NH_3/CH_4 combustion at various global equivalence ratios and CH_4 mass fractions. Global $\varphi > 1.25$ caused flame instability because the core recirculation zone was weaker. When $\varphi > 1.1$, the NO emission was very low (~20 ppm), mostly because amidogen radicals (NH_2^*) consumed most of the NO. On the other hand, carbon monoxide (CO) production was ~900 ppm when the global flame equivalence ratio exceeds 1.1. But in the fuel-lean combustion, reactions among the nitrogen atoms (N^*), imidogen (NH^*), and oxygen atoms (O^*), altogether with nitroxyl (HNO) + H (hydrogen atom) $\rightarrow$ NO + H_2, were identified as the main sources of NO production.

In another study, blending the NH_3 with CH_4 was reported to reduce NO production in the excess air operation to ~70 ppm/kW [7], which is substantially lower than the premixed combustion of ammonia/air where NO emission was ~151.5 ppm/kW [8]. When compared to the emissions performance of biodiesel, diesel, and natural gas, NH_3/CH_4 is still quite high [9,10]. Khateeb et al. [11] recently reported that when mixture input velocity and thermal power increased, the ammonia component in the fuel blend need to be reduced to ensure flame stability.

The non-premixed NH_3/CH_4 combustion under swirling flow and elevated atmospheric pressure conditions was studied by Somarathne et al. [12]. When the energy proportion of ammonia raised by 40%, The nitric oxide generation from NH_3/CH_4 non-premixed combustion surged by about three orders of magnitude. In another study [13], it was found that excess air non-premixed NH_3/CH_4 combustion resulted in encouraging NO mitigation. In contrast to premixed ammonia/air combustion, premixed ammonia/methane/air combustion lifted nitric oxide production by ~1.3 times. As opposed to non-premixed ammonia/air combustion, non-premixed ammonia/methane/air combustion lowered nitric oxide by a factor of ~2 [13]. Additionally, it was also unveiled that premixed ammonia/methane/air combustion produced

100 much greater nitrogen dioxide (NO_2) and nitrous oxide (N_2O) emissions than non-premixed

101 ammonia/methane/air combustion. It was presumed that the main mechanism for NO

102 generation during NH_3/CH_4 burning is due to fuel-bound nitrogen [13].

103 In a more recent study [14], the emission of premixed ammonia/methane/air swirl

104 flames was examined numerically by elevating the NH_3 mole fraction up to 60%. The NO

105 transport equation computed throughout the simulation is found to improve the NO emission.

106 The study showed that residence period, temperature, and nitrogenous components are crucial

107 determinants of NO concentration profile. For CH_4/NH_3 flames, the inner recirculation

108 residence time determines the NO level, and locally high NO concentration is mostly driven

109 by prolonged local residence time. The formation of OH^* and NO were tied to the high

110 temperature [14]. The investigation of the radical components unveils that HNO is the

111 primarily responsible for the important reaction route with regards to NO formation. The H, O,

112 and O_2 concentrations declined as the NH_3 fraction was raised (leading to elevated HNO

113 concentration). When the NH_3 mass fraction was increased to 40%, the NO production is the

114 highest among all cases examined [14].

115 Zhang et al. [15] examined the blow-off features of NH_3/air and NH_3/CH_4/air swirl

116 flames experimentally and numerically. The findings demonstrated that the ammonia swirl

117 flame exhibited weak lean flame stability that may be significantly enhanced by incorporating

118 CH_4 into the fuel. Furthermore, the lean blow-off limit for the NH_3 swirl flame does not appear

119 to be affected by the elevated swirl number. On the other hand, the swirl number for the 50

120 wt.% NH_3 flame results in an obvious extension of the lean blow-off limit. Four distinct flame

121 macrostructures responsible for eventual flame blow-off were identified when lowering the

122 NH_3/air and NH_3/CH_4/air flame global equivalence ratio. In all, the NH_3/air flame extinguished

123 much quicker than the NH_3/CH_4/air flame, which is mostly due to the excessive stretch that

124 results in local extinction during the blow-off process [15]. Despite studies that are dedicated

125   to examine and understand the fundamental combustion characteristics of NH_3/CH_4/air swirl

126   flames, the effects of carbon dioxide (CO_2) addition into NH_3/CH_4/air flame have not been

127   analysed yet. CH_4 and CO_2 are the major components in a typical biogas mixture that is

128   commonly produced via the anaerobic digestion of organic matter. Anaerobic digestion is

129   widely recognised as a more environmentally friendly way of producing renewable methane.

130   Considering the scarce understanding of NH_3/biogas swirl combustion, the present study aims

131   to examine it numerically. By using NH_3/CH_4 swirl combustion as baseline, the flame

132   temperatures, velocities, turbulent kinetic energy, premixed combustion regime, turbulent

133   Damkhöler number (Da), and turbulent flame speed for NH_3/biogas swirl flame are examined.

134

135

136

137

138

2.0   Research method

2.1 Construction of swirl burner

Figure 1a depicts the schematic diagram of a swirl burner with the integration of premixed gas to improve flame stabalisation. The plenum was designed for the premixing of fuel and air to attain a homogeneous gaseous mixture, then transfer towards the swirler to be combusted. The reference for the exit plane of the burner is $h = 0 \, mm$. The swirler hub has an internal diameter of 26 mm and an outer diameter of 40mm. The axial swirler comprises six straight vanes with a thickness of 1.5 mm and aligned $45°$ angle from the axial centerline axis, resulting in a geometric swirl number of roughly $S_N \sim 0.84$. The introduction of the swirl is to create a central toroidal recirculation zone (CTRZ) that enhances the mixing of combustion products with high thermal energy and unburned premixed reactants. This consequently promotes cleaner combustion whilst improving flame stabalisation. A quartz tube was placed on the exit plane's flange to visualise flames. The delivery system is depicted in Figure 1b. The dry air was delivered and controlled with a minimal deviation of 1.5% through a mass flow controller (Sierra). To replicate the biogas composition, CH_4 and carbon dioxide (CO_2) were delivered to the mixing chamber at a specific ratio. Mass flow controllers were employed to regulate the flow rate of CH_4 and CO_2 (Sierra, 1.5% full-scale accuracy). At the burner's exit, the mixture of air and fuel was ignited to establish the swirl flame.

2.2 Test procedures and operating conditions

Exhaust emissions like nitric oxide (NO), oxygen (O_2), and carbon dioxide (CO_2) were quantified by using a sampling probe connected to a gas analyser (KANE Quintox 905), and the sampling probe was placed 13 mm upstream from the quartz tube. The gas analyser can quantify NO, carbon monoxide (CO), O_2, and CO_2 in the ranges of 0-1000 ppm, 0-10,000 ppm, 0-25 %, and 0-99.9 %, respectively. The emission data were collected at five points radially

164 across the quartz tube outlet. By using the area-weighted average velocity approach [16], the

165 mean average of all emissions was computed from the five points readings collected. For this

166 study, a biogas composition of CH_4 (70 wt.%) blended with CO_2 (30 wt.%) was adopted. The

167 flow rates of CH_4, CO_2, and air were configured to establish the swirl flame at an input thermal

168 power of 7 kW and a global equivalence ratio of 0.8. The data collected was used for model

169 verification and validation.
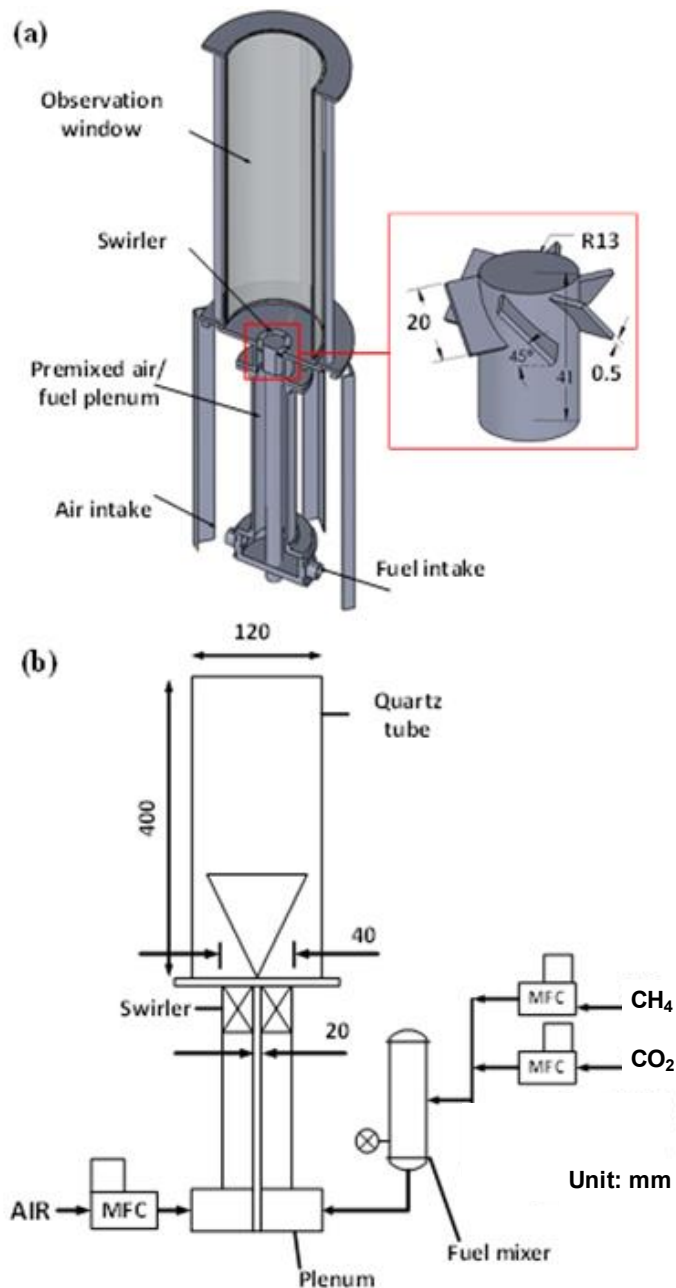
170
171 Figure 1 (a) The model of swirl burner and (b) schematic representation of the gas transport
172 system. (Reprinted from [16] with permission from Elsevier)

2.3 Numerical modelling

2.3.1 Flamelet generated manifold (FGM)

The flamelet is simulated using a comprehensive chemistry reaction scheme in the FGM approach. The present work employed the Gas Research Institute mechanism (GRIMECH 3.0 - GRI 3.0) scheme (53 species, 325 reactions) as a chemical kinetics reaction mechanism. The FGM technique employs the chemistry from a laminar flamelet database built from many 1D flamelet computations done with full chemical kinetics and transport equations. The type of flamelet (premixed or non-premixed) is decided based on the boundary conditions of each flamelet, which vary somewhat. The premixed swirl flame was modelled in this work with the software - ANSYS Fluent. A one-dimensional premixed flamelet was constructed to solve the flamelets in reaction progress space. The following equation defines the variable reaction progress:

$$c = \frac{[\sum_k \alpha_k (Y_k - Y_k^u)]}{[\sum_k \alpha_k (Y_k^{eq} - Y_k^u)]} = \frac{Y_c}{Y_c^{eq}} \tag{1}$$

The progress variable is defined as a normalised sum of the mass fraction of the product species across all species in the chemical process. From equation (1), Y_k represents the mass fraction of the kth species, u represents the unburned reactant at the flame input, and eq represents chemical equilibrium at the flame exit. Accordingly, the coefficient α_k is provided so that the flame's reaction rate, c, grows monotonically. $\alpha_k = 0$ for all species, with the exception of $\alpha_{CO_2} = \alpha_{CO} = 1$ for hydrocarbon combustion and $\alpha_{H_2O} = 1$ for fuels containing no C element, such as H_2. The adiabatic flamelet equations in one dimension can be translated from physical-space to reaction-progress space.

$$\rho \frac{\partial Y_k}{\partial t} + \rho \frac{\partial Y_k}{\partial c} \dot{\omega}_c = \rho \chi_c \frac{\partial^2 Y_k}{\partial c^2} + \dot{\omega}_k \tag{2}$$

8

$$\rho\frac{\partial T}{\partial t}+\rho\frac{\partial T}{\partial c}\dot\omega_c=\rho\chi_c\frac{\partial^2 T}{\partial c^2}-\frac{1}{c_p}\sum_k h_k\dot\omega_k+\frac{\rho\chi_c}{c_p}\left(\frac{\partial c_p}{\partial c}+\sum_k c_{p,k}\frac{\partial Y_k}{\partial c}\right)\frac{\partial T}{\partial c} \qquad (3)$$

where Y_k is the kth species mass fraction, T is the temperature, ρ is the density of the fluid, t is time, $\dot\omega_k$ is the kth species mass fraction rate, h is the total enthalpy and $c_{p,k}$ is the kth species specific heat at constant pressure. The definition of the scalar dissipation rate χ_c is:

$$X_c=\frac{\lambda}{\rho c_p}|\nabla c|^2 \qquad (4)$$

Where λ corresponds to heat conductivity. Variable with c, the scalar dissipation χ_c is an input to the equation set, where Equation 4 corresponds to:

$$\rho\frac{\partial Y_k}{\partial t}+\rho\frac{\partial Y_k}{\partial c}\dot\omega_c=\frac{\lambda}{c_p}|\nabla c|^2\frac{\partial^2 Y_k}{\partial c^2}+\dot\omega_k \qquad (5)$$

Other than the progress variable, the mixture fraction in FGM corresponds directly to the single equivalence ratio of the 1D premixed flamelet. The maximum scalar dissipation, χ_{max}, of a premixed flamelet at varying mixture fractions is distinct. Modelling the scalar dissipation $\chi_c(f,c)$ at any mixture fraction f as

$$\chi_c(f,c)=\chi_{max}^{STO}\exp\left(-2\left(er\,fc^{-1}\left(\frac{f}{f_{STO}}\right)\right)^2\right)\exp\left(-2\left(er\,fc^{-1}(2c)\right)^2\right) \qquad (6)$$

where STO represents the stoichiometric proportion of the mixture and $er\,fc^{-1}$ is the inverse complimentary error function. The only model input to the premixed flamelet generator in ANSYS Fluent is the scalar dissipation at stoichiometric mixture fraction, X_{max}^{sto}. The solution of unstrained (freely propagating) physical space flamelets for rich, lean, and stoichiometric hydrocarbon and H_2 flames at standard temperature and pressure [16] often matches the default value of $X_{max}^{sto} = 1000/s$ s.

9

2.3.2 Grid setup

To achieve a reliable simulation result, the numerical grid setup is vital. Location with high temperature and possible species concentration requires high-quality components with a slow development rate. As depicted in Figure 2, the cut shell approach, which largely comprises of a structured hexahedron grid, was selected for this simulation investigation. The minimum and the maximum number of cells in the grid are 0.7 and 1 million, respectively. Aspect ratio and orthogonal quality determined the quality of the mesh. According to Zerrin et al. [17], a hexahedron grid with a maximum aspect ratio of 35 and a minimum orthogonal quality of 0.15 is of high quality. In this instance, the highest aspect ratio was 13.43 and the minimum orthogonal quality was 0.19, which falls within the range specified by Zerrin and colleagues [17]. Near the burner outlet, a denser grid of cells was formed, while the grid grew coarser as it approached the burner outlet. At the exit of the burner, a refined mesh is required to predict the occurrence of high velocity, species, and temperature gradient.
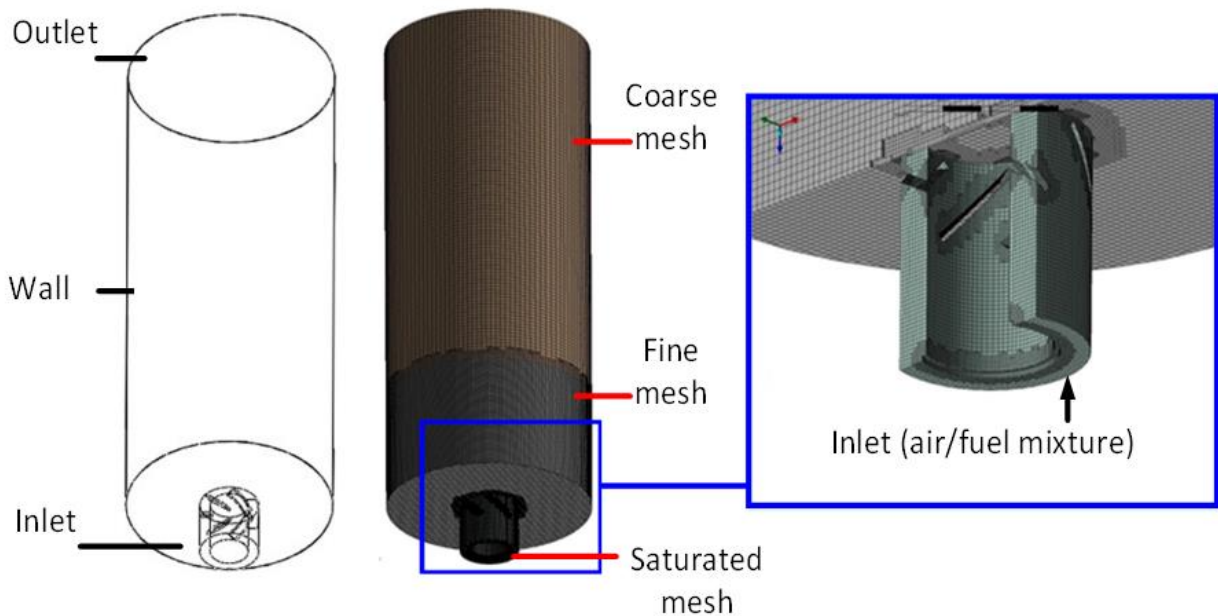
Figure 2 The simulation setting of boundary conditions and mesh setup. (Reprinted from [16] with permission from Elsevier)

2.3.3 Fuel compositions and boundary conditions

As stated in Table 1, several biogases/ammonia compositions were used as operational fuels in this simulation. Based on these compositions, a mass flow rate model setup was built at the inlet. Simulations were performed at an input thermal power of 7 kW and $\varphi = 0.8$. The turbulence intensity and hydraulic diameter at the fuel input were set to 5% and 10 mm, respectively. The turbulence intensity value is derived from the value indicated by Krieger, et al. [18]. The combustor wall was assumed to be a no-slip boundary and species flux is absent. Flow outlet at the exit of the burner was regarded as the burner outlet condition. At the outlet boundary, the static pressure was set to atmospheric surrounding pressure.

Table 1 CH_4, CO_2, and NH_3 mass fraction in the premixed biogas/NH_3.

Biogas composition		NH_3 wt.% in biogas/NH_3 mixture	Acronym
CH_4 wt.% in biogas	CO_2 wt.% in biogas		
100%	0%	20%	C0N20
100%	0%	30%	C0N30
100%	0%	40%	C0N40
70%	30%	20%	C30N20
70%	30%	30%	C30N30
70%	30%	40%	C30N40
60%	40%	20%	C40N20
60%	40%	30%	C40N30
60%	40%	40%	C40N40

2.3.4 Convergence criteria

The grid independence test was performed using various numbers of elements, as shown in Figure 3a. The NO emissions for biogas converges at 1.7 million elements, irrespective of the variation in global equivalence ratio from 0.9 to 0.75. The grid number of 1.7 million was deemed grid-independent since the results were nearly comparable to those of the >1.8 million scenario. Several criteria reported by earlier scholars were used to determine the convergence of a solution. Mayr et al. [19,20] claim that the simulation is deemed to converge if the fluctuations of maximum temperature is <5 K and species concentration is <0.001 mol fraction. The residuals for mixture fraction variance and mean mixture fraction should be reduced to less than 10^{-6}, whereas the residuals for other equations, such as continuity, velocity, and k-epsilon are less than 10^{-3} [19,20]. In addition to residual, the number of iterations is also an indicator of the convergence of simulation process. As depicted in Figure 3b, the variations in NO emission have no obvious changes after 5000 iterations. As the NO value fluctuates minimally and enters a steady state, the NO_x mean value is regarded to have converged. Figure 3c and Figure 3d show that flame shape obtained via numerical simulation resemble that captured during the experimental work. A notable feature in 2D swirl flame image is the formation of High Momentum Flow Region (HFMR) at burner outlet. Such feature is also shown in previous studies involved swirl flames [16,21].

2.3.5 Fluid flow modelling

The mass, momentum, energy, and heat transfer equations were solved in this investigation using ANSYS Fluent with finite volume. For steady-state conditions, a pressure-based solver was utilized. Solving the RANS (Reynold-averaged Navier Stokes) equations describes the fluid flow. To close the RANS equations, turbulence models were used. In the Computational Fluid Dynamics (CFD) code, several turbulence models are provided. The

273   standard k- model was used for the turbulence model in this simulation. The pressure-velocity

274   coupling was calculated using a SIMPLE computational technique [19,20]. The governing

275   equations for momentum, turbulent kinetic energy and dissipation rate, progress variable, and

276   mixture fraction are discretised using a second-order upwind approach. The PRESTO! system

277   is implemented for pressure. Mayr et al. [19,20] reported that the PRESTO! technique

278   expedites simulation convergence.

279
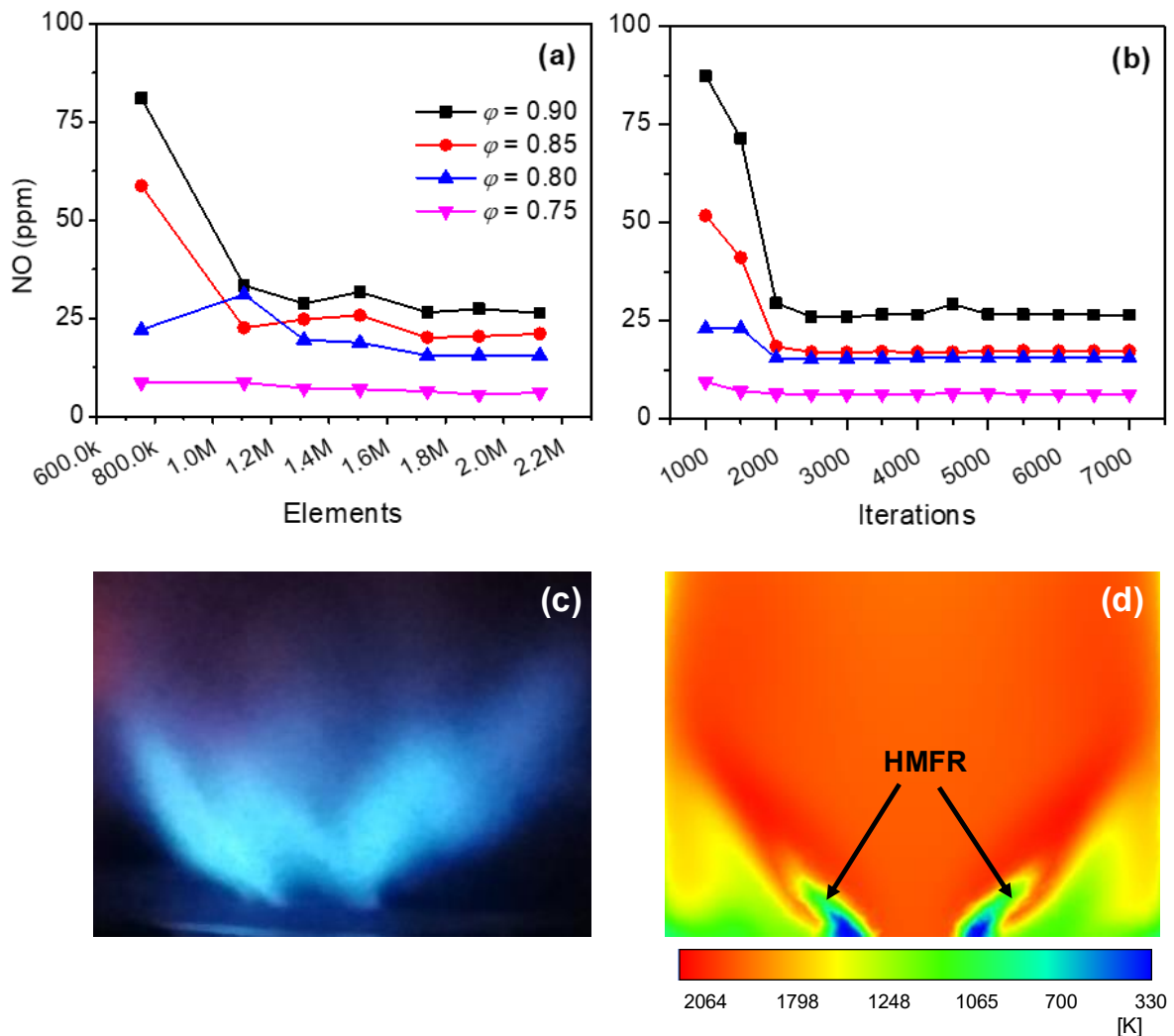
280

281   Figure 3 Emission of NO from biogas at 7 kW input thermal power as a function of (a) grid or
282   mesh element size, and (b) the number of iterations. Biogas swirl flame images (7 kW input
283   thermal power, $\varphi = 0.8$) obtained via (c) experiment, and (d) numerical simulation.

284

285   Figure 4a compares the experimental data with the estimated NO emissions by the FGM

286   models at various equivalence ratios. It has been noted that the FGM-estimated NO

287   concentration exhibits a tendency that is comparable to that of experimental data. At lean

288   regions, prediction by the FGM technique demonstrated good agreement with experimental

289   results, particularly at equivalence ratios of 0.85 and below. However, when stoichiometry was

290   approached, the concentration of NO was much over anticipated. A similar trend was also

291   observed by [16]. Premixed FGM's divergence from experimental data is mostly attributable

292   to the species' inability to disseminate in the direction of the Z gradient. Thus, one of the

293   variables causing the variation in NO concentration is the absence of the diffusion effect in the

294   premixed FGM model [22].

295   As can be shown in Figure 4b, the deviation of the CO_2 species predicted by the FGM

296   model from the actual experimental value is often less than 10%. However, when the

297   equivalency ratio becomes closer to stoichiometric, the FGM technique underestimates the CO_2

298   emissions. According to Najafi-Yazdi et al. [23], the mass fraction is decomposed before

299   considerable heat release, hence the progress variable frequently produces erroneous findings

300   for rich mixes. Figure 4c demonstrates that the FGM technique accurately predicts the O_2

301   species since the error percentage is less than 10% for all equivalence ratios. For quick chemical

302   processes, the FGM technique primarily use quasi-steady state approximation, and this method

303   is ideally suited to forecast free radical species like O_2 [24].

304

305
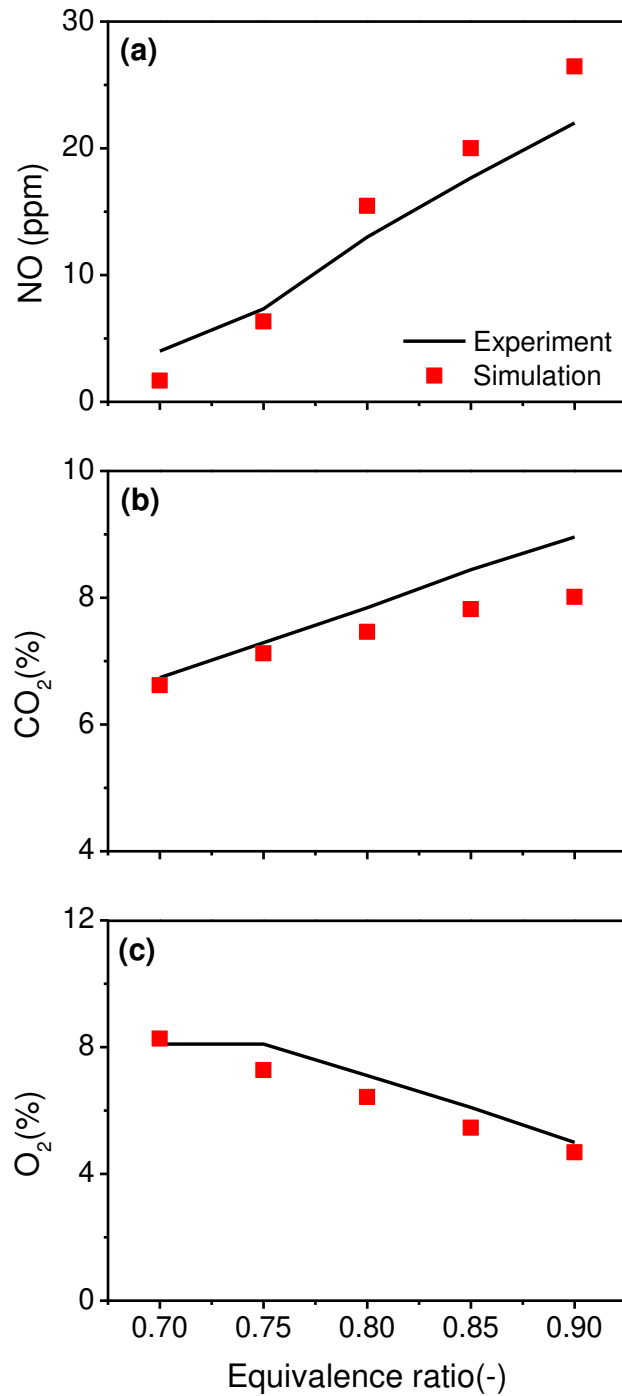
306
307 Figure 4 (a) NO, (b) CO_2, and (c) O_2 emissions of biogas combustion at 7 kW input thermal
308 power obtained from experiments and numerical simulations using FGM method as a function
309 of equivalence ratio.

310

311

3.0   Result and discussion

Figure 5a shows that for the fuel mixture with 20 wt.% NH_3, the flame temperature reduces by averaging 150 K as CO_2 wt.% increases from 0% to 40% at 20 mm downstream. In addition to the flame temperature reduction, the peak temperature is also shifted radially outwards, and the dual temperature peak are apparent when CO_2 wt.% increases to 40%. A similar temperature profile deformity is advanced to a lower CO_2 wt.% when NH_3 wt.% in the reactant increases to 30% and 40%, as shown in Figure 5b and Figure 5c. Figure 6 illustrates the dual peak temperature by comparing flame temperature profiles with normalised OH^* intensity. It is shown that the peak OH^* is present at nearly the same location where the temperature peak is found (C0N40). With elevated CO_2 mass fraction, dual peak OH^* is formed and aligns with the radial position of dual peak temperature.

For fuel mixture without CO_2 infusion (i.e., C0N20, C0N30, and C0N40), peak temperature takes place at a radial position ~35 mm for 20 mm downstream, regardless of the variation in NH_3 mass fraction. Thus, the displacement of peak temperature to an outer radial position at elevated CO_2 wt.% suggests that a portion of the premixed reactant mixture is not consumed at the inner branch of the reaction zone. Conversely, it is carried to an outer branch of the reaction zone by the positive radial velocity of the swirling flow. At 30 mm downstream (Figure 5d-f), the peak temperature for all fuel mixture is stretched radially by another ~5 mm. This is primarily due to the expansion of the swirling flow diameter farther downstream. Meanwhile, increased NH_3 mass fraction in the absence of CO_2 (i.e., C0N20, C0N30, and C0N40) does not result in dual peak temperature at 20 mm downstream. This denotes that CO_2 is the main contributor to the dual peak temperature formation, seemingly because of CO_2 decelerates the reaction rate that hinders the establishment of uniform reaction across the HFMR. At 30 mm downstream (Figure 5d-f), the dual peak temperature diminishes despite the radial displacement of peak temperature remains illustrious. The shifting of peak temperature

16

337 to the outer branch and the existence of multiple reaction zones due to the addition of secondary

338 fuel were also observed in a study pertaining to n-heptane/natural gas dual fuel swirl flame

339 [25]. The flame peak temperature at a 15 mm burner downstream was split up and shifted by

340 ~5 mm radially outwards when natural gas was added to the n-heptane swirl flame. Moreover,

341 the dual peak was also seen in the normalised OH^* signal at 5 mm and 15 mm downstream,

342 respectively. For neat n-heptane swirl flames, however, no double peak temperature was

343 observed [25]. Premixing the CO_2 into the CH_4/NH_3 blend has resulted in notable change in

344 flame temperature radial profiles, especially at near burner outlet. The addition of CO_2 tends

345 to stretch the peak temperature radially outwards and demands an extended downstream

346 distance to develop a more uniform reaction radially across the HMFR.

347
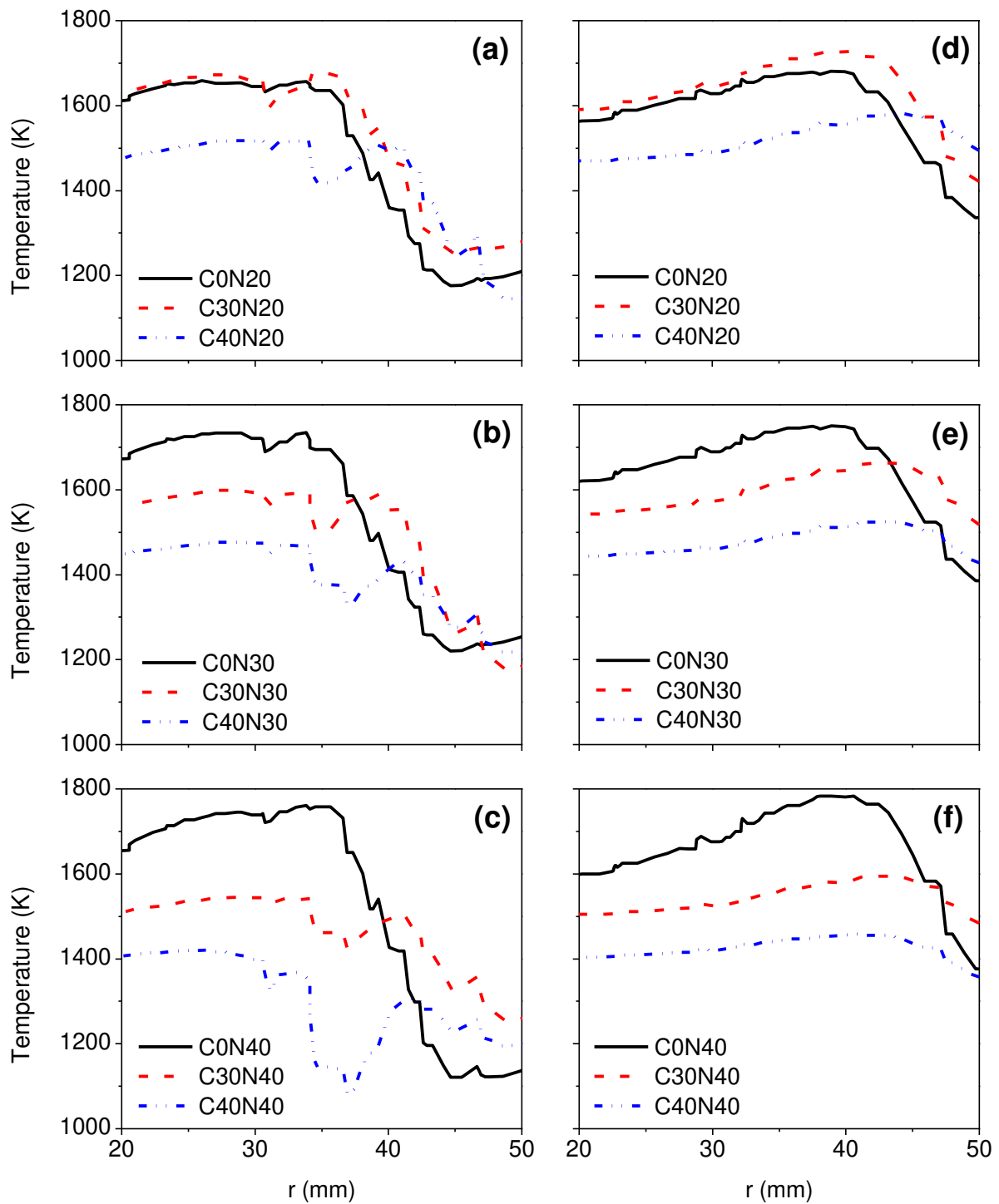
348
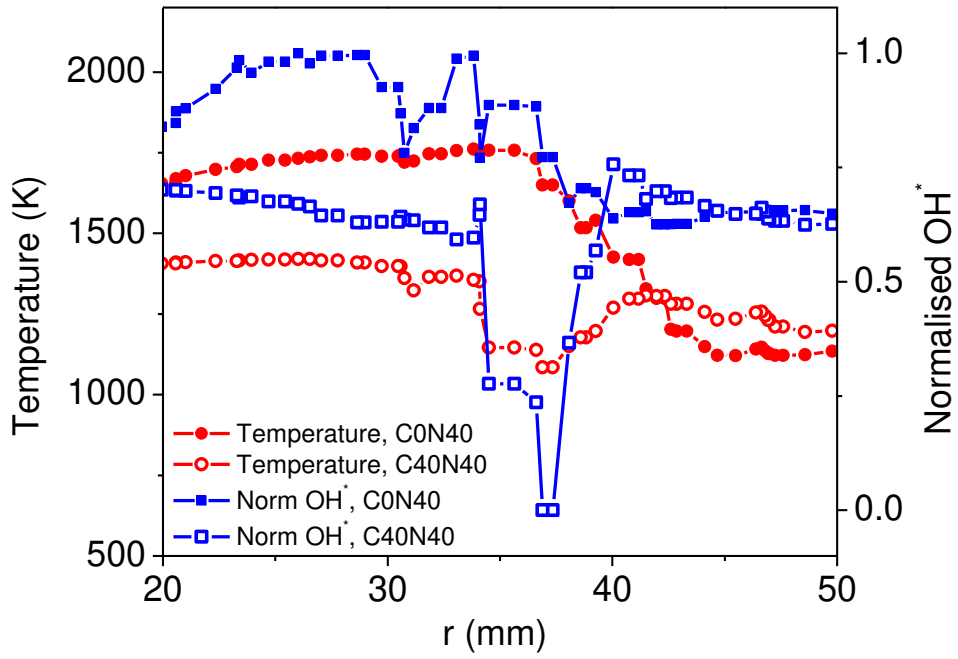349 Figure 5 Flame temperature radial profiles for $CH_4/NH_3/CO_2$ premixed combustion (7 kW
350 input thermal power, $\varphi = 0.8$) at (a-c) 20 mm, and (d-f) 30 mm downstream from the burner
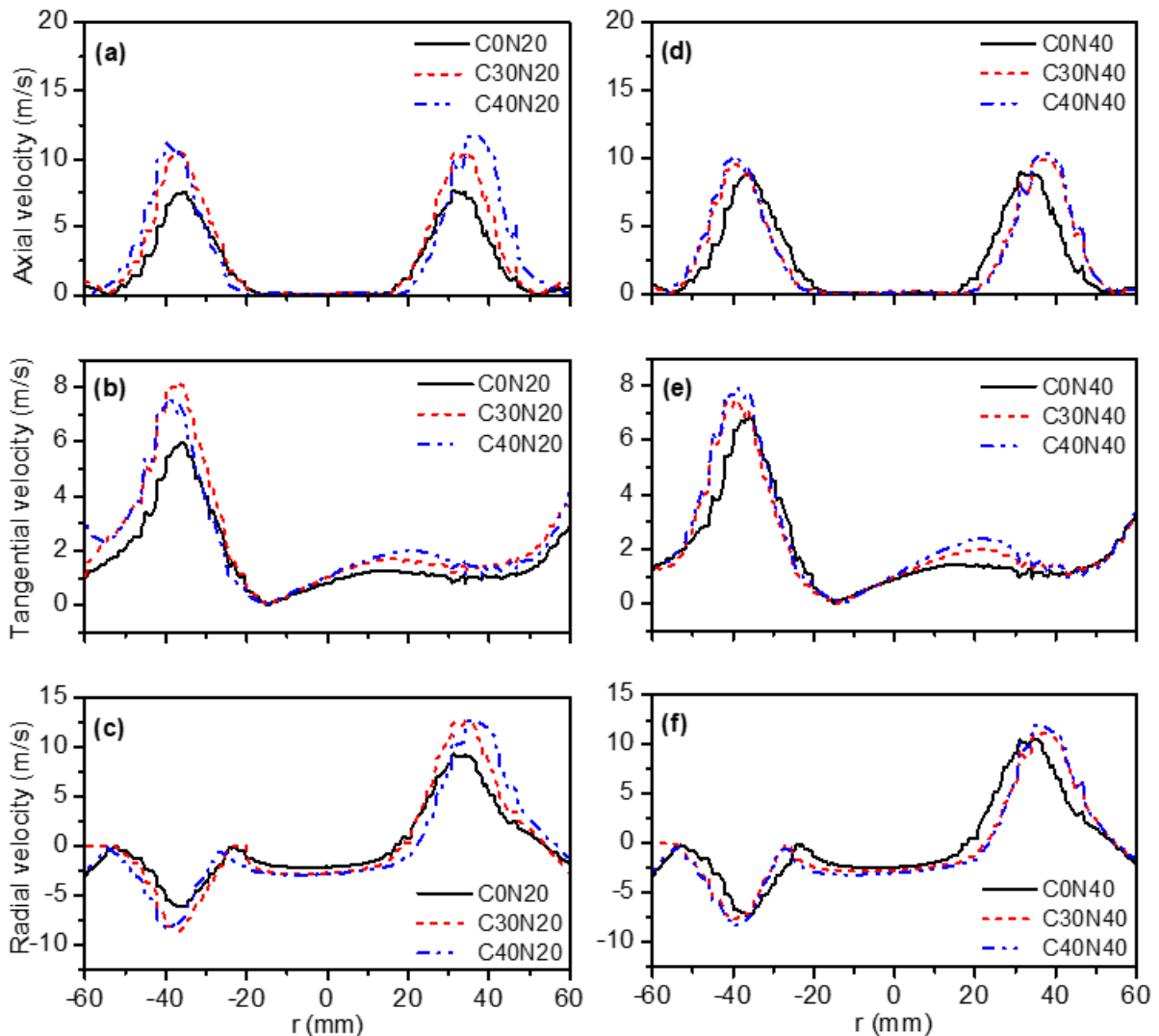351 outlet.

352

Figure 6 Normalised OH^* and temperature radial profiles for $CH_4/NH_3/CO_2$ premixed combustion (7 kW input thermal power, $\varphi = 0.8$) at 20 mm downstream from the burner outlet.

359   Figure 7 shows that peak velocities (axial, radial, and tangential) are concentrated

360   within the HMFR. It can be observed also that the peak velocities for fuel mixture with 40 wt.%

361   CO_2 is overall higher than 0% CO_2 by averaging 6 m/s, irrespective of the variation in NH_3

362   mass fraction. The introduction of CO_2 has also altered the size and turbulent kinetic energy of

363   the structure as depicted in Figure 8, whereas the turbulent kinetic energy for the CH_4/NH_3 is

364   notably lower than the CO_2-infused fuel mixtures. Increased CO_2 mass fraction not only

365   elevates turbulent kinetic energy, but it also shifts peak turbulent kinetic energy and velocities

366   radially outward by ~10 mm.

367
368   Figure 7 Velocities profiles of $CH_4/NH_3/CO_2$ premixed combustion (7 kW input thermal power,
369    $\varphi = 0.8$) at 20 mm downstream from the burner outlet.

370
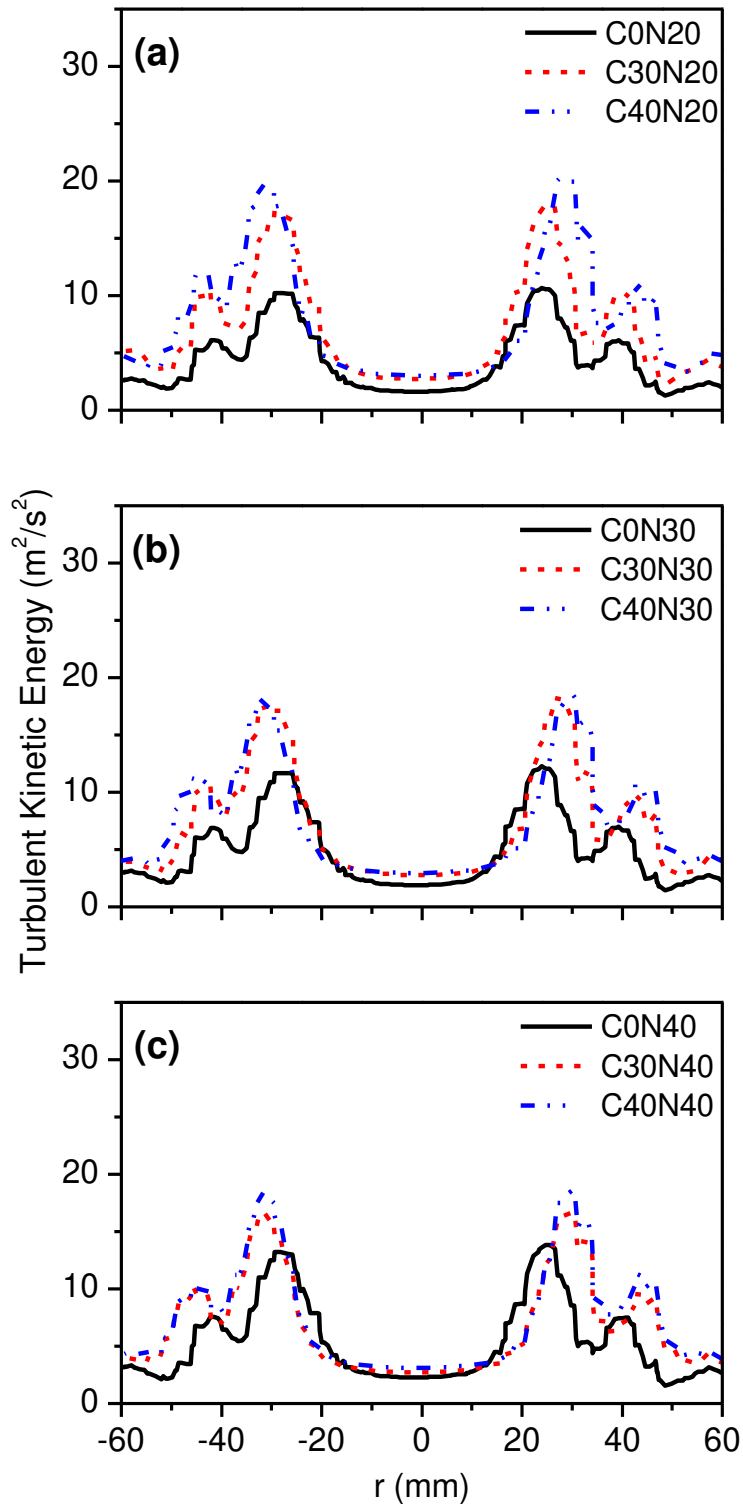
Figure 8 Turbulent kinetic energy for $CH_4/NH_3/CO_2$ premixed combustion (7 kW input thermal power, $\varphi = 0.8$) at 20 mm downstream from the burner outlet.

376 With reference to Figure 5, increased CO_2 wt.% leads to an averaging lower flame

377 temperature, owing to the less released chemical energy. Thus, the elevation of gas velocities

378 and turbulent kinetic energy due to the increased CO_2 wt.% are apparently not because of the

379 increased heat release rate. As illustrated in Figure 9, increased CO_2 wt.% directs the premixed

380 combustion into the thin reaction zone where the fluctuation is becoming more prominent than

381 flame laminar propagating speed. Aggravated flame fluctuation leads to the persistent local

382 flame quenching and reignition. The eddies of premixed reactant mixture that receive an influx

383 of heat from active species are ignited and burned irregularly, depending on the eddy size and

384 local mixture composition [26]. This promotes the formation of a combustion wave that

385 consequently gives rise to the gas velocities and turbulent kinetic energy as indicated in Figure

386 7 and Figure 8, respectively. The O_2/CO_2 volumetric ratio has consequential effects on flame

387 fluctuation. As O_2/CO_2 decreased from 35% to 31% (i.e., increased CO_2 volume fraction in the

388 premixed reactant), the heat release fluctuation for a CH_4 swirl flame increased by ~90% [27].

389 Although lowering the O_2/CO_2 to < 31% resulted in relative peak fluctuation amplitude

390 reduction by ~40%, this was accompanied by a wider band peak with multiple peaks resided,

391 denoting the flame started to fluctuate at a wider bandwidth prior to its extinction at 21%

392 O_2/CO_2 volumetric ratio [27]. Increased CO_2 wt.% in the premixed reactant mixture tends to

393 provoke flame fluctuation, and this basically promotes the development of a combustion wave

394 which in turn raises the gas velocities and turbulent kinetic energy.

395 Figure 7 also shows that radial velocity has reduced noticeably when landing on the

396 left-hand side of the reaction zone. The radial velocity on the right is ~12 m/s, decreasing its

397 value on the left to ~8 m/s, a reduction of ~33%. On the contrary, the tangential velocity at the

398 left-hand side of the reaction zone is remarkably higher than that at the right, showing an energy

399 tradeoff between radial and tangential velocities in the flow field whereby the radial flow

400 momentum is transferred to raise tangential velocity that consequently set up the swirl flow

401   motion to anchor the flame right at the top of the burner outlet. In other study [28], the axial

402   velocity gradient increased notably right at the vicinity of Central Toroidal Recirculation Zone

403   (CTRZ) and the HMFR on the right-hand side of the swirl flame, but its magnitude on the left-

404   hand side of the swirl flame was ~50% lower than that of the right-hand side, signifying flow

405   momentum exchange in the swirling flow field [28].

406
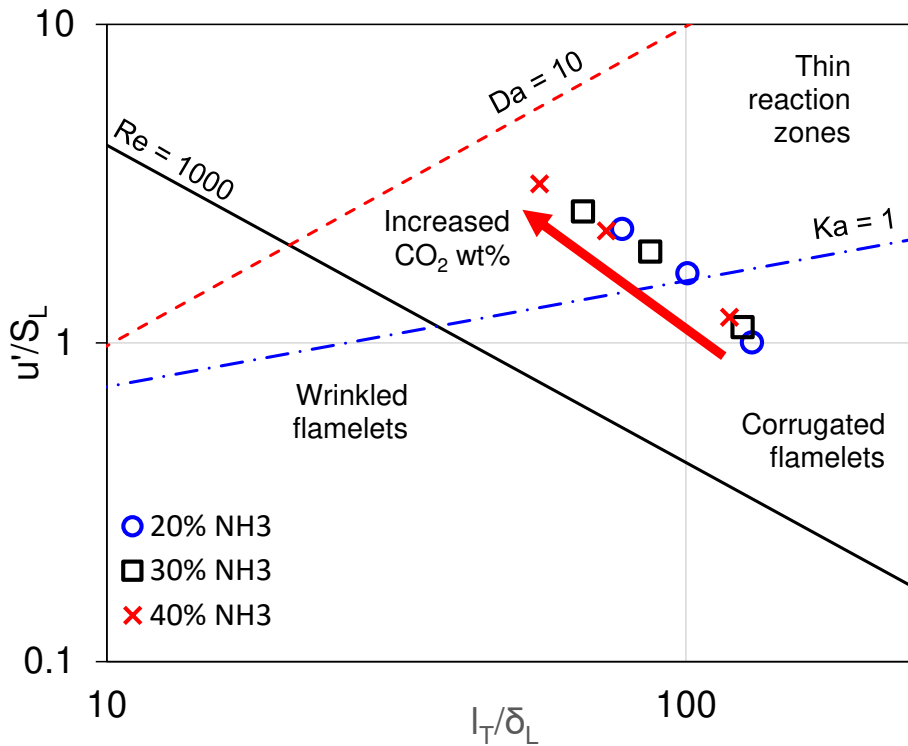
407
408   Figure 9 Regimes of $CH_4/NH_3/CO_2$ premixed turbulent combustion (7 kW input thermal power,
409     $\varphi = 0.8$) in the Borghi diagram.

410

411

412

413   Figure 10 shows that the turbulent Damkhöler number for the methane/ammonia is

414 considerably higher than the premixed reactant mixture with 30 wt.% and 40 wt.% CO_2 by

415 ~40%. In all cases, notably high Da takes place at the central region of the reaction zone and

416 declines radially outwards. The increase in length scales of the flame and the fall in turbulence

417 intensity cause the Da to grow in the central region. Increased length scales of the flow are

418 reflected in Figure 7 where flow velocities are minimal in the central region of the reaction

419 zone. The length scales decline near the boundary of CTRZ and HMFR, owing to the elevated

420 turbulent intensity in this region and this, in turn, lowers the Da [26]. O'Doherty and Gardner

421 [28] study on swirling flow demonstrated that a wide range of eddies appeared in the vicinity

422 of the CTRZ and the HMFR. These eddies promote rigour mixing and at the same time elevate

423 turbulent intensity in this region [28].

424   Meanwhile, increased CO_2 wt.% reduces the Da drastically at the central region of the

425 combustor, this is mainly because of the substantial reduction in laminar flame speed with

426 increasing CO_2 mass fraction (Figure 11b). A similar tendency is also observed when the NH_3

427 mass fraction is raised, owing to the decline in the laminar flame speed and increased flame

428 thickness. Owing to the lower NH_3/air burning rate, the thickness of the reaction zone for

429 NH_3/air stoichiometric laminar flame under atmospheric conditions is wider than CH_4/air by a

430 factor of approximately 12 [6]. A secondary peak of Da is observed at the near-wall area,

431 despite it is considerably lower than Da at the central region. Like the central region, the Da

432 for methane/ammonia is distinctively higher than the premixed reactant mixture with CO_2

433 infusion. The elevation of CO_2 mass fraction in the premixed methane/ammonia fuel mixture

434 has inherently led to a significant reduction in Da, mainly due the decline in mixture reactivity.

435
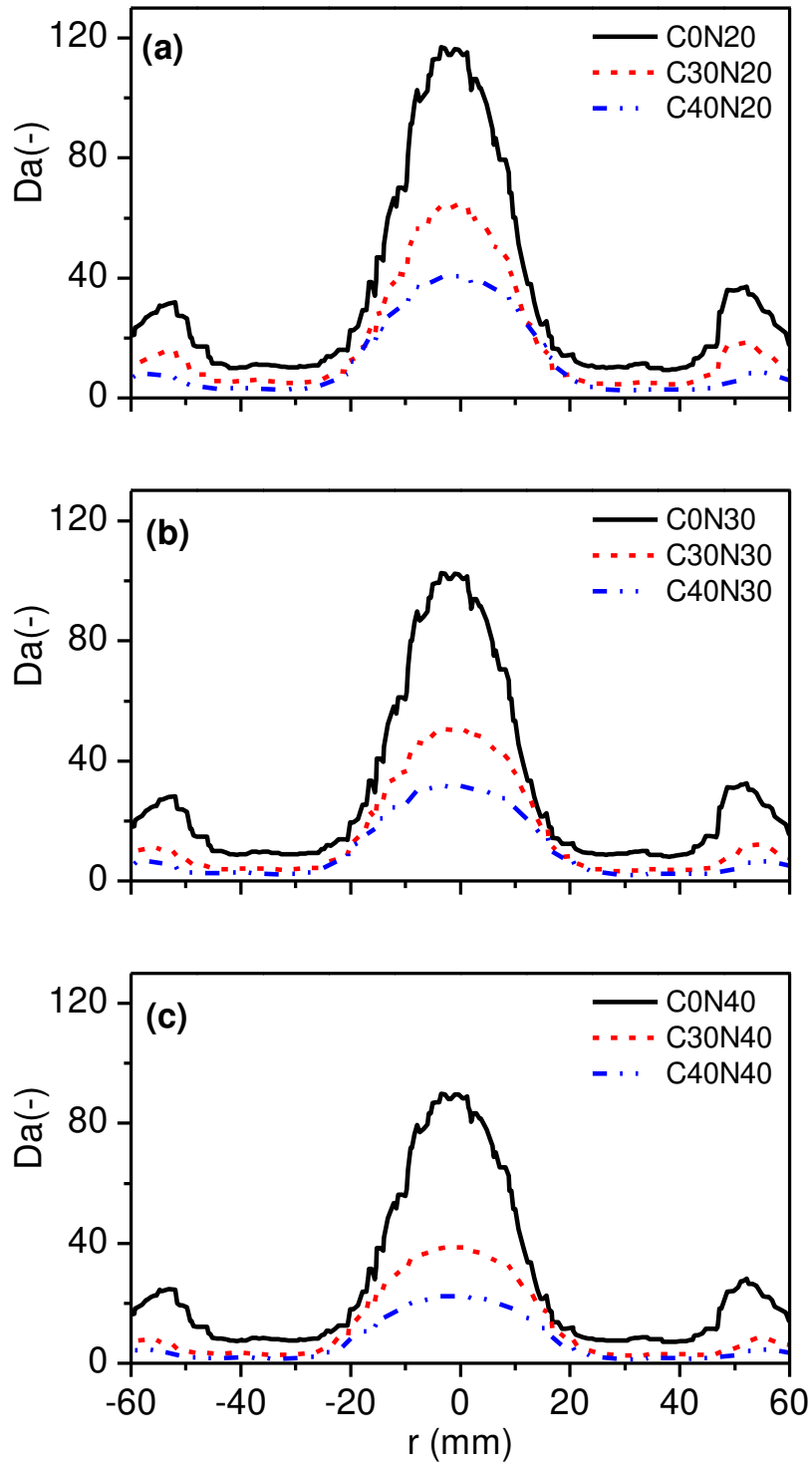
Figure 10 Da radial profile for $CH_4/NH_3/CO_2$ premixed combustion (7 kW input thermal power, $\varphi = 0.8$) at 20 mm downstream from burner outlet.

443   Figure 11a illustrates that normalised turbulent flame speed increases in a linear fashion

444   with normalised turbulent intensity below 1.5. As normalised turbulent intensity goes beyond

445   1.5, the increase of normalised turbulent flame speed turns out to be somewhat steeper.

446   Furthermore, CH_4/NH_3 mixture with a higher CO_2 mass fraction results in a noticeably higher

447   normalised turbulent flame speed than a fuel mixture with a lower CO_2 mass fraction. Likewise,

448   increased NH_3 mass fraction also leads to an increased normalised turbulent flame speed when

449   the CO_2 mass fraction in the fuel mixture is fixed. Elevated normalized turbulent flame speed

450   is postulated because of the magnified combustion pulsation when CO_2 and NH_3 mass fractions

451   are escalated. As shown in Figure 9, the wrinkling flamelet is diminishing with higher levels

452   of turbulent intensity. The idea of a coherent flame front would no longer be valid in this case,

453   and the combustion is preserved almost exclusively by the reactions established at the interface

454   of fresh mixture' eddies and hot combustion active species. Depending on the composition of

455   the mixture and the magnitude of the local turbulence intensity, the flow of heat and active

456   species consume each eddy at an irregular rate. Intensified flow pulsations are produced in this

457   way, elevating the gas flow velocities and turbulent flame speed as a result. The influence of

458   small turbulent eddies are consequential, it was demonstrated that when the proposed numerical

459   model considered small turbulent eddy effects on the flame front, the estimated turbulent flame

460   speed was more closely matched to the measured values, indicating the significance of small-

461   scale turbulent eddies that enter the preheating layer of the premixed flame front in affecting

462   the normalised turbulent flame speed [29]. A fragmented flame front at higher turbulent

463   intensity generates pressure pulsation that overall elevates the normalised turbulent flame speed.

464   Figure 11b, however, shows that the laminar flame speed declines with the rise of

465   turbulent intensity. This ascertains that the increased S_T/S_L in Figure 11a is predominantly

466   because of the exaggerated flow pulsations but not because of the increased reactivity when

467   turbulent intensity is amplified. The reduction in S_L, on the other hand, can be attributed to the

468 flame stretching as flow momentum increased especially in the fuel-lean operation. The flame

469 surface for the fuel-lean CH_4/air premixed turbulent flame was found to expand by a factor of

470 approximately 3 as Reynolds number (Re) was raised by an order of magnitude [30]. With

471 inflated flame stretching, the heat loss turns out more prominent than heat generation, and this

472 leads to the laminar flame speed reduction as a result.

473
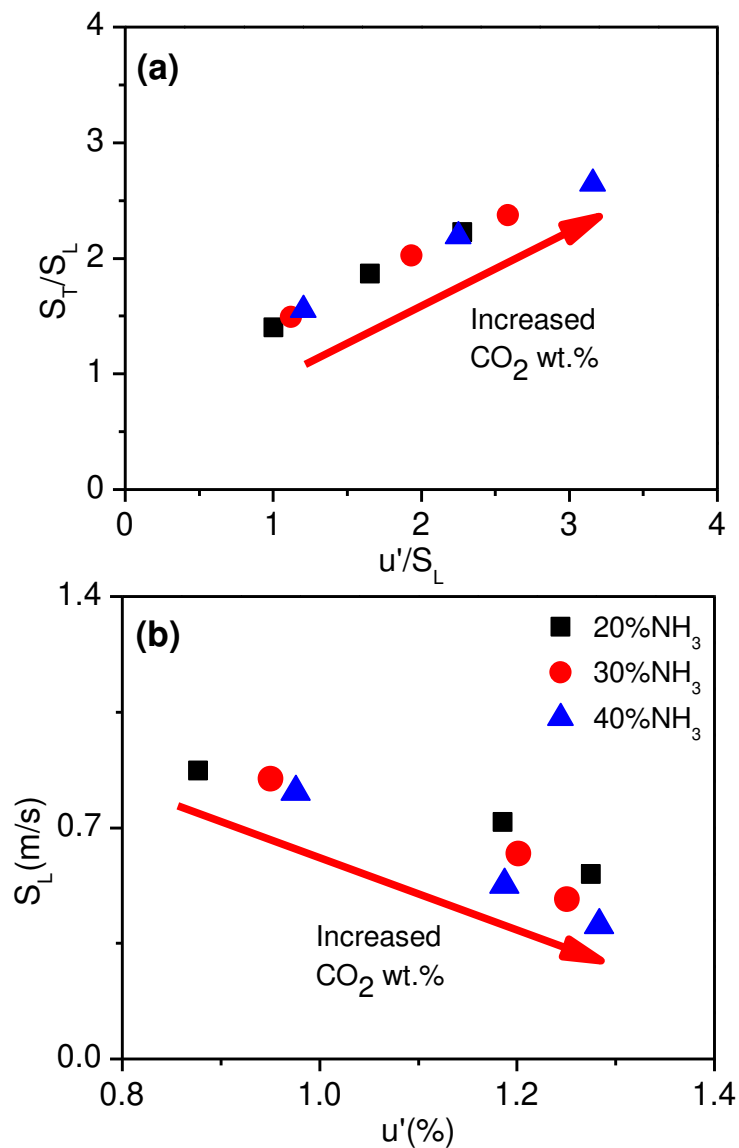
474
475 Figure 11 (a) Normalised turbulent flame speed vs normalised turbulent intensity, and (b)
476 Laminar flame speed vs turbulent intensity for CH_4/NH_3/CO_2 premixed combustion (7 kW
477 input thermal power, $\varphi = 0.8$).

4.0   Conclusion

The fundamentals swirl combustion characteristics of CH_4/NH_3 under elevated CO_2 addition and at a global equivalence ratio of 0.8 were examined. A commercial CFD package was employed to model the flow domain and simulate the physics of the reacting swirl flow. The numerical results were verified and validated using emissions data obtained via in-house experimental works. This study unveils that the introduction of CO_2 has profound effects on CH_4/NH_3 combustion characteristics. Increased CO_2 mass fraction to 40 wt.% in the premixed CH_4/NH_3 mixture lowers the peak flame temperature by 150-400 K on average as compared to the 0 wt.% CO_2 case. Moreover, the peak temperature is stretched by ~5 mm radially outwards and visible radial temperature profile deformation is observed particularly in the upstream region. These are mainly due to the reduction in reactivity of the premixed reactant mixture with elevated CO_2 wt.%. The reduction in mixture reactivity is also reflected in the peak Da reduction by a factor of ~1.5 when CO_2 wt.% increases from 0% to 40%.

Furthermore, increased CO_2 wt.% also directs the premixed combustion from corrugated flamelet into thin reaction flamelet, primarily because of the turbulent fluctuation has prevailed over the laminar flame propagation significantly. Increased flow pulsation due to the elevated CO_2 wt.% raises the flow velocities and turbulent kinetic energy visibly. Furthermore, aggravated flow pulsation also has a prominent effect on turbulent flame propagation. Despite a drastic reduction in laminar flame speed, the normalised turbulent flame speed has increased by a factor of 1.6 when CO_2 wt.% is raised from 0% to 40%, corresponding to an increase of u'/S_L from 1 to 3. Overall, the escalation of normalised turbulent flame speed is mostly due to the exaggerated flow pulsation instead of the increased heat release rate at elevated CO_2 wt.%. The use of biogas (CH_4/CO_2 mixture) to replace neat CH_4 for co-combustion with NH_3 is expected to incur intensified flow pulsation, the fluctuation intensity is likely to exacerbate as NH_3 wt.% in the biogas/NH_3 mixture is increased > 40%. There is a

28

503   lot of room for system optimisation going forward, especially with appropriate choice of swirl

504   number, preheating temperature, and elevated atmospheric pressure.

505

506

Acknowledgment

References

[1]   Valera-Medina A, Banares-Alcantara R, editors. Techno-Economic Challenges of
      Green Ammonia as an Energy Vector. Elsevier; 2021.

[2]   The Royal Society. Ammonia : fuel and energy store 2020.

[3]   Valera-Medina A, Xiao H, Owen-Jones M, David WIF, Bowen PJ. Ammonia for
      power. Prog Energy Combust Sci 2018;69:63–102.
      https://doi.org/10.1016/j.pecs.2018.07.001.

[4]   Newhall HK, Starkman ES. Theoretical Performance of Ammonia as a Gas Turbine
      Fuel. SAE Trans 1967;75:772–84.

[5]   Verkamp FJ, Hardin MC, Williams JR. Ammonia combustion properties and
      performance in gas-turbine burners. Symp Combust 1967;11:985–92.
      https://doi.org/10.1016/S0082-0784(67)80225-X.

[6]   Kobayashi H, Hayakawa A, Somarathne KDKA, Okafor EC. Science and technology
      of ammonia combustion. Proc Combust Inst 2019;37:109–33.

[7]   Valera-Medina A, Marsh R, Runyon J, Pugh D, Beasley P, Hughes T, et al. Ammonia–
      methane combustion in tangential swirl burners for gas turbine power generation. Appl
      Energy 2017;185:1362–71.

[8]   Hayakawa A, Arakawa Y, Mimoto R, Somarathne KDKA, Kudo T, Kobayashi H.
      Experimental investigation of stabilization and emission characteristics of ammonia/air
      premixed flames in a swirl combustor. Int J Hydrogen Energy 2017;42:14010–8.

[9]   Chiong MC, Valera-Medina A, Chong WWF, Chong CT, Mong GR, Mohd Jaafar
      MN. Effects of swirler vane angle on palm biodiesel/natural gas combustion in swirl-
      stabilised gas turbine combustor. Fuel 2020;277:118213.
      https://doi.org/10.1016/j.fuel.2020.118213.

[10] Chong CT, Chiong MC, Ng JH, Lim M, Tran MV, Valera-Medina A, et al.
      Oxygenated sunflower biodiesel: Spectroscopic and emissions quantification under
      reacting swirl spray conditions. Energy 2019;178:804–13.
      https://doi.org/10.1016/j.energy.2019.04.201.

[11] Khateeb AA, Guiberti TF, Zhu X, Younes M, Jamal A, Roberts WL. Stability limits
      and NO emissions of technically-premixed ammonia-hydrogen-nitrogen-air swirl
      flames. Int J Hydrogen Energy 2020;45:22008–18.
      https://doi.org/10.1016/j.ijhydene.2020.05.236.

[12] Somarathne KDKA, Okafor EC, Sugawara D, Hayakawa A, Kobayashi H. Effects of

549   OH concentration and temperature on NO emission characteristics of turbulent non-

550   premixed CH 4 /NH 3 /air flames in a two-stage gas turbine like combustor at high

551   pressure. Proc Combust Inst 2020;000:1–8.

552   https://doi.org/10.1016/j.proci.2020.06.276.

553 [13] Okafor EC, Somarathne KDKA, Hayakawa A, Kudo T, Kurata O, Iki N, et al.

554   Towards the development of an efficient low-NOx ammonia combustor for a micro

555   gas turbine. Proc Combust Inst 2019;37:4597–606.

556   https://doi.org/10.1016/j.proci.2018.07.083.

557 [14] An Z, Zhang M, Zhang W, Mao R, Wei X, Wang J, et al. Emission prediction and

558   analysis on CH4/NH3/air swirl flames with LES-FGM method. Fuel

559   2021;304:121370. https://doi.org/10.1016/j.fuel.2021.121370.

560 [15] Zhang M, Wei X, Wang J, Huang Z, Tan H. The blow-off and transient characteristics

561   of co-firing ammonia/methane fuels in a swirl combustor. Proc Combust Inst

562   2021;38:5859–68. https://doi.org/10.1016/j.proci.2020.08.056.

563 [16] Afzanizam N, Tung C, Ng J, Tran M, Chyuan H, Valera-medina A. ScienceDirect

564   Experimental and numerical studies on the premixed syngas swirl flames in a model

565   combustor. Int J Hydrogen Energy 2019;44:24126–39.

566   https://doi.org/10.1016/j.ijhydene.2019.07.158.

567 [17] Turkeli-ramadan Z, Sharma RN, Raine RR. Two-dimensional simulation of premixed

568   laminar fl ame at microscale. Chem Eng Sci 2015;138:414–31.

569   https://doi.org/10.1016/j.ces.2015.08.026.

570 [18] Krieger GC, Campos AP V, Takehara MDB, Alfaia F, Veras CAG. Numerical

571   simulation of oxy-fuel combustion for gas turbine applications. Appl Therm Eng

572   2015;78:471–81. https://doi.org/10.1016/j.applthermaleng.2015.01.001.

573 [19] Mayr B, Prieler R, Demuth M, Hochenauer C. The usability and limits of the steady fl

574   amelet approach in oxy-fuel combustions 2015;90:1478–89.

575   https://doi.org/10.1016/j.energy.2015.06.103.

576 [20] Mayr B, Prieler R, Demuth M, Potesser M, Hochenauer C. CFD and experimental

577   analysis of a 115 kW natural gas fired lab-scale furnace under oxy-fuel and air – fuel

578   conditions. Fuel 2015;159:864–75. https://doi.org/10.1016/j.fuel.2015.07.051.

579 [21] Sidey J, Mastorakos E. Visualisation of turbulent swirling dual-fuel flames. Proc

580   Combust Inst 2017;36:1721–7.

581 [22] Verhoeven LM, Ramaekers WJS, Oijen JA Van, Goey LPH De. Modeling non-

582   premixed laminar co-flow flames using flamelet-generated manifolds. Combust Flame

583   2012;159:230–41. https://doi.org/10.1016/j.combustflame.2011.07.011.

584   [23]   Najafi-yazdi A, Cuenot B, Mongeau L. Systematic definition of progress variables and

585   Intrinsically Low-Dimensional , Flamelet Generated Manifolds for chemistry

586   tabulation. Combust Flame 2012;159:1197–204.

587   https://doi.org/10.1016/j.combustflame.2011.10.003.

588   [24]   Oijen JA Van, Goey LPH De. Predicting NO Formation with Flamelet Generated

589   Manifolds n.d.

590   [25]   Evans MJ, Sidey JAM, Ye J, Medwell PR, Dally BB, Mastorakos E. Temperature and

591   reaction zone imaging in turbulent swirling dual-fuel flames. Proc Combust Inst

592   2019;37:2159–66. https://doi.org/10.1016/j.proci.2018.07.076.

593   [26]   Law CK. Combustion Physics. Cambridge University Press; 2006.

594   [27]   Khalil AEE, Gupta AK. Flame fluctuations in Oxy-CO2-methane mixtures in swirl

595   assisted distributed combustion. Appl Energy 2017;204:303–17.

596   https://doi.org/10.1016/j.apenergy.2017.07.037.

597   [28]   Vigueras-Zuniga MO, Valera-Medina A, Syred N, Bowen P. High Momentum Flow

598   Region and Central Recirculation Zone Interaction in Swirling Flows. Ing Mec

599   Technol Y Desarro 2014;4:195–204.

600   [29]   Gülder ÖL. Contribution of small scale turbulence to burning velocity of flamelets in

601   the thin reaction zone regime. Proc Combust Inst 2007;31 I:1369–75.

602   https://doi.org/10.1016/j.proci.2006.07.189.

603   [30]   Luca S, Attili A, Lo Schiavo E, Creta F, Bisetti F. On the statistics of flame stretch in

604   turbulent premixed jet flames in the thin reaction zone regime at varying Reynolds

605   number. Proc Combust Inst 2019;37:2451–9.

606   https://doi.org/10.1016/j.proci.2018.06.194.

607

608

609

610

611

612

613